Comprehensive validation of three-dimensional finite element modelling of wheel-rail high-frequency interaction via the V-Track test rig

Zhang, Pan; He, Chunyan; Shen, Chen; Dollevoet, Rolf; Li, Zili

DOI
10.1080/00423114.2024.2304626

Publication date
2024

Document Version
Final published version

Published in
Vehicle System Dynamics

Vehicle System Dynamics
International Journal of Vehicle Mechanics and Mobility

ISSN: (Print) (Online) Journal homepage: https://www.tandfonline.com/loi/nvsd20

Comprehensive validation of three-dimensional finite element modelling of wheel-rail high-frequency interaction via the V-Track test rig

Pan Zhang, Chunyan He, Chen Shen, Rolf Dollevoet & Zili Li

To cite this article: Pan Zhang, Chunyan He, Chen Shen, Rolf Dollevoet & Zili Li (18 Jan 2024): Comprehensive validation of three-dimensional finite element modelling of wheel-rail high-frequency interaction via the V-Track test rig, Vehicle System Dynamics, DOI: 10.1080/00423114.2024.2304626

To link to this article: https://doi.org/10.1080/00423114.2024.2304626

Published online: 18 Jan 2024.

VEHICLE SYSTEM DYNAMICS
https://doi.org/10.1080/00423114.2024.2304626

Comprehensive validation of three-dimensional finite element modelling of wheel-rail high-frequency interaction via the V-Track test rig

Pan Zhang, Chunyan He, Chen Shen, Rolf Dollevoet and Zili Li

Section of Railway Engineering, Delft University of Technology, Delft, the Netherlands

ABSTRACT

Wheel-rail high-frequency interaction is closely related to the formation of railway short-wave defects. Finite element (FE) method has been widely used to simulate wheel-rail dynamic systems, but its validity in modelling high-frequency interaction has not been fully demonstrated in three dimensions (3D). This work aims at comprehensively validating the 3D FE modelling of wheel-rail high-frequency interaction using a downscale V-Track test rig. First, the FE model of the V-Track is developed that comprehensively includes the 3D track elasticity. The simulated track dynamic behaviours are validated against hammer tests, and the major vibration modes are analyzed employing modal analysis. Afterwards, the simulate wheel-rail dynamic responses are comprehensively compared with measurement results up to 10 kHz. Their characteristic frequencies are identified and correlated to the eigenmodes of the vehicle-track system. The results indicate that the proposed 3D FE model is capable of comprehensively and accurately simulating the 3D track dynamics and wheel-rail dynamic interaction of the V-Track up to 10 kHz. Rail vibrations dominate the wheel-rail dynamic contact within 10 kHz, while the wheel vibrations play an increasingly important role at higher frequencies and become decisive near the wheel eigenmode frequencies. The V-Track overall achieves dynamic similarity to the real vehicle-track system.

ARTICLE HISTORY
Received 3 August 2023
Revised 11 December 2023
Accepted 8 January 2024

KEYWORDS
Wheel-rail dynamic system; high-frequency interaction; 3D finite element modelling; comprehensive validation; vibration modes; V-Track test rig

1. Introduction

In recent decades, the railway has become one of the most popular transport modes worldwide because of being safe, green and efficient. Railway trains keep evolving toward the higher speed and the heavier axle load to meet the increasing demand for a shorter travel time and a larger transport capacity. With increased train speeds and axle loads, various short-wave defects have occurred on the wheels and rails with higher probability, such as short pitch rail corrugation, squats, and wheel polygonisation [1–5]. They excite large wheel-rail impact force, induce fierce vibration and noise, and further accelerate the deterioration of the vehicle-track system, which considerably increases the maintenance

CONTACT Zili Li z.li@tudelft.nl

Supplemental data for this article can be accessed online at https://doi.org/10.1080/00423114.2024.2304626.

cost. The formation of the short-wave defects is closely related to the wheel-rail dynamic interaction [6–10], especially in the high-frequency range (i.e. 1.5 kHz [11]). To identify their formation mechanisms and develop the corresponding countermeasures, a good understanding of wheel-rail high-frequency interaction is needed.

Numerous models have been developed to simulate wheel-rail dynamic interaction in the literature. W. Zhai *et al.* [12–14] propose a classical vehicle-track coupled model that considers the vehicle and the track as an integral system coupling through wheel-rail contact, which has been widely used to understand and optimise the railway dynamic system [15–18]. D. Thompson *et al.* [19,20] developed a dynamic model to investigate wheel-rail noise where the wheel and the rail structural vibrations excited by the surface roughness have been treated in detail. J.C. Nielsen *et al.* [21] simulated dynamic wheel-rail interaction with flexible wheelsets and moving track models and validated it against field wheel-rail contact force measurement. It was reported that track flexibility is important in the wheel-rail interaction and wheelset flexibility is also significant in the lateral wheel-rail interaction. X. Jin [22,23] developed a three-dimensional (3D) train-track model with a modification of Kalker's non-Hertzian rolling contact theory to study rail corrugation in a curved track and found that the initial corrugation with a fixed wavelength is gradually erased by wheel-rail interaction instead of growing. Most models in the literature simulate the wheel as a rigid body and the rail as a beam and they are coupled together by Hertzian or non-Hertzian contact [24–27]. However, L. Baeza *et al.* [28] pointed out that wheel flexibility plays an important role in the high-frequency wheel-rail dynamics and the corrugation calculation results indicate that a rigid wheel model may misinterpret the corrugation wavelength-fixing mechanism. C. Shen [29] compared the simulated frequency response functions (FRFs) of a rail beam model with the experimental results from the hammer test and concluded that the beam model is only accurate up to 800 Hz. Besides, the half-space assumption of the Hertz theory may not hold when dealing with non-steady wheel-rail contact at short-wave corrugation and squats [9,30,31]. Therefore, an advanced model that can more accurately simulate the high-frequency dynamics and contact mechanics of the wheel-rail system is necessary to better understand and mitigate the short-wave defects and their induced vibration and noise.

With the development of computation power, the finite element method (FEM) has been increasingly employed to model wheel-rail dynamic interaction at track discontinuities (i.e. crossings [32] and rail joints [33,34]) and wheel and rail defects (i.e. wheel flat [35] and polygonisation [36], rail corrugation [9,37] and squats [38,39]). Compared to other methods, FEM is capable of reproducing high-frequency dynamic effects in the wheel-rail interaction by including the continuum dynamics of the wheel and the rail. Meanwhile, it has the advantages of handling arbitrary contact geometries and nonlinear material properties to provide more accurate contact solutions [40]. In the literature, the FEM of wheel-rail dynamic interaction has been validated in terms of wheel-rail frictional rolling contact solutions [41,42], axle box acceleration (ABA) [43,44] and track vibrations [45,46]. However, these validation efforts have been performed in different models with diverse boundary conditions and parameters. Whether one model using the FEM can simultaneously match the global responses of the wheel-rail system remains unknown. One of the possible difficulties here is the lack of synchronous measurement data in the field. Besides, most FE models only considers the vertical track elasticity, such as the vertical fastening and ballast stiffness, without including the lateral and longitudinal track elasticity. This

simplification may cause unrealistic simulations of wheel-rail dynamic interaction in these two directions, which need to be further improved by comprehensively including 3D track elasticity.

To experimentally investigate wheel-rail dynamic interaction, an innovative downscale test rig called 'V-Track' has been developed in the laboratory. Compared to the existing testing facilities, the V-Track can better simulate the high-frequency dynamics of the vehicle-track system by the detailed treatment of wheel/rail material and geometry and the inclusion of important track and vehicle structural components [47] (see Figure 1). Many sensors have been installed in the V-Track that enables us to synchronously acquire the dynamic responses of the wheel-rail system in a controllable environment, including wheel-rail contact forces [48], ABA, and track vibration velocities and accelerations. Besides, the hammer, 3D Handyscan and hardness tests can be performed in the V-Track to gain insights into the vehicle and track dynamic behaviours, wheel and rail profiles and hardness changes [49]. Some typical defects, such as rail corrugation [49] and head checks [50], were successfully reproduced and studied using the V-Track. The corresponding mitigation approaches to these defects can be developed and tested.

This work aims to comprehensively validate the 3D FEM via the V-Track test rig and contribute to a better understanding of wheel-rail high-frequency interaction. The paper is organised as follows. Section 2 develops a 3D FE wheel-rail interaction model of the V-Track. Section 3 compares the dynamic behaviours of the curved and straight track, validates the 3D track dynamics by hammer tests, and analyzes the eigenmodes of the track employing modal analysis. Section 4 comprehensively validates the simulated responses against the measured pass-by rail accelerations, wheel-rail contact forces and ABA up to 10 kHz in three directions, and identifies the characteristic frequencies of the wheel-rail dynamic interaction. Section 5 further discusses the simulation results and the dynamic similarity between the V-Track and the real wheel-rail system. Section 6 draws the main conclusions.

2. 3D FE wheel-rail interaction model of the V-Track

In this section, the structure and main components of the V-Track are first briefly introduced (Section 2.1), and the corresponding 3D FE model of the V-Track is developed to simulate the wheel-rail dynamic interaction (Section 2.2).

2.1. Structure of the V-Track

The current V-Track configuration shown in Figure 1 is approximately 1/5 scale of the real vehicle-track system, consisting of two wheel assemblies mounted on the ends of the main frame, running over a ring track system, as shown in Figure 1a. Figure 1b depicts the structure and main components of one wheel-track system in detail. The cylindrical wheel is cut from real Dutch railway wheel and has a diameter of 130 mm. It is connected to a guiding block through an axle box. The wheel, axle box and guiding block together are movable vertically along two guiding shafts under the preloads of primary suspension springs. The spring stiffness in total is 230 N/mm, and the preload is adjustable from 0 to 7500 N by changing the initial compression of the springs. The angle of attack (AoA) of the wheel is also adjustable between $-2°$ and $+2°$ by rotating the axle box around its vertical

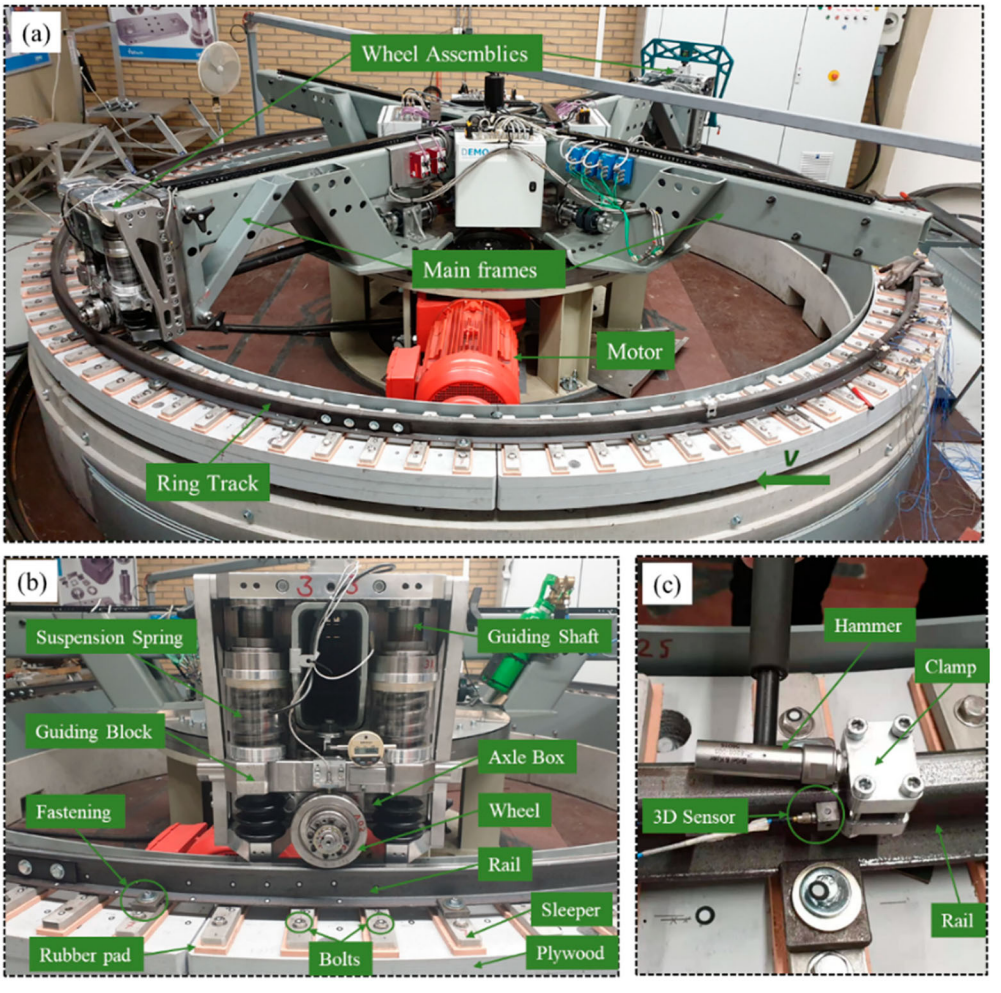

Figure 1. The downscale wheel-rail dynamic interaction test rig named 'V-Track'. (a) Structure of the V-Track, consisting of two wheel assemblies running on a ring track system; (b) main components of the V-Track; (c) setup for the pass-by rail acceleration measurement and the hammer test. The clamp is designed for the longitudinal excitation of the track.

axis. There are two motors in the V-Track. One drives the main beam to rotate so that the wheel assemblies run along the ring track with a maximum speed of 40 km/h. The other applies a controllable torque to the wheels. If the torque and AOA are zero, the wheels will in principle run as free wheels on the rail, mimicking the wheels of a trailer railway wagon on a straight track. Depending on the direction of the torque, desired braking or traction force is generated at the wheel-rail contact. Other vehicle components above the primary suspension, such as the bogie, secondary suspension and car body, are not included in the V-Track because of their insignificant influence on wheel-rail high-frequency vibrations [11].

The ring track has a diameter of 4 m and consists of four sections of S7 rails connected by four rail joints; each section is a quarter of the ring and is 3.14 m long. The rails are

constrained on steel sleepers by fastenings, as shown in Figure 1b. In total, 100 sleepers are used with an average sleeper span of 125 mm. The clips of fastenings are installed every three or four sleepers to induce relatively strong dynamic excitation to the wheel-rail system. The sleepers are fixed with bolts on plywood layers that are used to simulate the subgrade. Between sleepers and plywood layers are rubber pads which reproduce the elasticity and damping of ballast layers in real tracks. The rail inclination is approximately 0 to achieve wheel-rail contact in the middle of the rail head.

In the test, the loading condition of the V-Track is designed to simulate wheel-rail dynamic interaction on straight tracks. The wheel preload is set to 4500 N, equivalent to the field axle load of about 11.25 t based on the similarity law [47,51], with a maximum contact pressure of 1.15 Gpa. The similarity law is a common scaling method to relate the scale rig to its full-size equivalence [47,51]. A torque of 23 N.m is applied to generate a adhesion coefficient of around 0.08. The AoA is set to be a small value of about 2 mrad. The wheel rolling speed is 13 km/h. Dynamometers are in the wheel assemblies to continuously measure the wheel-rail contact forces in the vertical, longitudinal and lateral directions [48]. Three 1D accelerometers are placed on the wheel axle box to measure the ABA in three directions. The pass-by rail accelerations at the 75th sleeper are measured in three directions by a 3D sensor, as shown in Figure 1c. Hammer tests are also performed at this sleeper to obtain the dynamic behaviours of the track system; the vertical and lateral excitation positions are on the rail head and gauge face, respectively, as close as possible to the 3D sensor. The longitudinal excitation is applied using a self-made clamp (see Figure 1c). A 3D HandyScan test [49] is conducted to measure the geometry and surface roughness of the rail and the wheel.

2.2. 3D FE modelling of the V-Track

A 3D FE wheel-rail interaction model of the V-Track is developed in ANSYS software, as shown in Figure 3. The axes X, Y, and Z refers to the longitudinal (rolling), lateral and vertical directions, respectively. The wheel, rail and sleepers are modelled based on their real geometries and materials using 8-node solid elements. Nonuniform meshing is employed to achieve computation efficiency, and the finest meshing size is in the solution zone and is 0.2 mm to ensure calculation accuracy for the wheel-rail rolling contact [41]. The axle box and guiding block are together modelled by mass elements. The primary suspension is modelled by spring-damper elements with an initial compression to apply a wheel preload of 4500 N. Compared to the models in the literature [38,40,43,45], this work extends the fastenings and the ballast models (rubber pads beneath the sleeper in Figure 1b) from one-dimensional to three-dimensional spring-damper elements, as shown in Figure 2a. In this manner, not only the vertical track elasticity, but also the longitudinal and vertical ones are included to more realistically simulate the track dynamics and further the wheel-rail dynamic interaction. The parameters of fastenings and ballast (i.e. stiffness and damping) are calibrated by best fitting the simulated track dynamics to those measured from hammer tests [52]. They are listed in Table 1 together with the nominal material properties of the wheel, the rail and the sleeper. The track model is 3.14 m long, corresponding to one of the 4 rail sections. Both curved and straight tracks are modelled to investigate the effect of the rail curvature (the 4-meter diameter) on the track dynamics, as shown in Figure 2b.

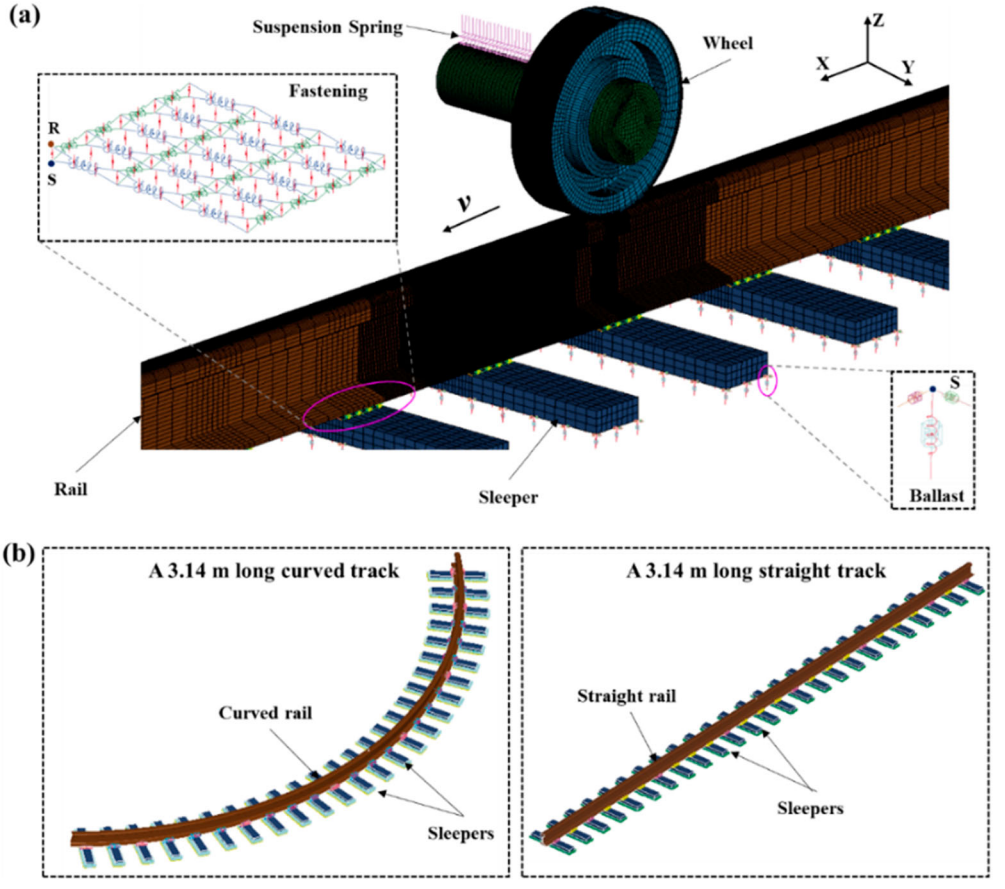

Figure 2. 3D FE wheel-rail dynamic interaction model of the V-Track. (a) Overview of the 3D FE model, including the suspension spring, wheel, rail, fastenings, sleepers and ballast elasticity. The letters 'R', 'S', '*v*' represent rail nodes, sleeper nodes and wheel speed, respectively. (b) the curved and straight track models with a length of 3.14 m. They are used to investigate the effect of the rail curvature on track dynamics.

The wheel-rail contact model applied an automatic surface-to-surface contact scheme based on the penalty contact algorithm [53]. The coefficient of friction is 0.35. The measured surface geometry from the 3D HandyScan test is adopted in the model to reproduce a realistic wheel-rail contact. An implicit-explicit sequential approach is employed to minimise the solution time and the dynamic effects during the initialisation of wheel-rail interaction. In the explicit calculation, the initial translation velocity of 3.61 m/s (13 km/h) and rotation velocity of 55.56 rad/s are prescribed to the wheel. The same initial translation velocity is applied to the suspension spring, axle box and guiding block. A braking torque of 23 N.m and a small AoA of 2 mrad was also applied to the model, generating a longitudinal braking force of about 230 N and a lateral force of about 100 N. This loading condition was designed to simulate the 3D wheel-rail dynamic interactions on the tangent track. The integration time step was sufficiently small (15 ns) to guarantee convergence and ensure the stability of the integration and the contact solution [54].

Table 1. Values of parameters in the 3D FE wheel-rail model of the V-Track.

Components	Parameter	Value
Wheel, rail, sleeper	Young's modulus	210 GPa
	Poisson's ratio	0.3
	Density	7850 kg/m^3
Suspension	Vertical stiffness	230 kN/m
	Vertical damping	100 N.s/m
Fastening	Vertical stiffness	290 MN/m
	Vertical damping	5.5 kN.s/m
	Longitudinal stiffness	45 MN/m
	Longitudinal damping	3.4 kN.s/m
	Lateral stiffness	36 MN/m
	Lateral damping	6.9 kN.s/m
Rubber pad (ballast)	Vertical stiffness	17 MN/m
	Vertical damping	500 N.s/m
	Longitudinal stiffness	1.5 MN/m
	Longitudinal damping	175 N.s/m
	Lateral stiffness	15 MN/m
	Lateral damping	300 N.s/m

3. Validation of 3D track dynamics

In this section, we first numerically compare the vibration characteristics of the straight and curved free rail in terms of frequency-wavenumber dispersion relations and vibration modes (Section 3.1). Afterwards, the simulated curved and straight track dynamics in the vertical, longitudinal and lateral directions are validated against the hammer tests (Section 3.2). During this process, the track dynamic parameters (i.e. railpad stiffness and damping) are calibrated, and the major track vibration modes are identified employing a modal analysis.

3.1. Comparison of the vibration characteristics of the straight and curved free rail

Figure 3 shows the wavenumber-frequency dispersion relations of the straight and curved free rail calculated by the same method as in [55]. Six wave modes are obtained within 10 kHz, which are vertical bending (I), longitudinal compression (II), lateral bending (III), lateral torsion (IV), web 1st bending (V), and web 2nd bending (VI) modes. respectively. It can be seen that the dispersion relations of the curved rail overall matches well with those of the straight rail, indicating the insignificant influence of the current rail curvature on the vibrational waves. Some slight deviations are observed in the vertical bending waves (I) and lateral torsion waves (IV) at frequencies lower than 1.5 kHz (indicated by the yellow boxes), which is caused by their mode coupling due to the rail curvature [56,57]. Meanwhile, a non-zero cut-on frequency of the longitudinal compression waves (II) is observed with the curved rail, which is commonly referred to the breathing or ring mode [56,57], caused by the coupling between the lateral movement and axial compression in a curved beam. These deviations will be reduced by the fastening constraints, which suppress and decouple rail vibrational waves [46]. Figure 4 further shows some examples of the rail vibration modes in the vertical, longitudinal and lateral directions. Both the mode frequencies (*mf* in short) and shapes are almost the same in the curved and straight rails, as long as their profiles, materials and lengths are identical.

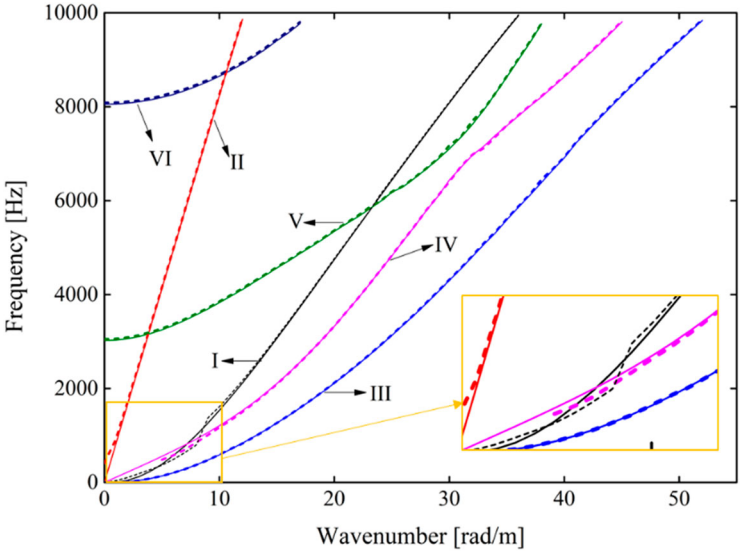

Figure 3. The wavenumber-frequency dispersion relations of the straight (solid lines) and curved (dashed lines) free rail. In this figure, 'I' refers to vertical bending waves, 'II' longitudinal compression waves, 'III' lateral bending waves, 'IV 'lateral torsion waves, 'V' web 1st bending waves, and 'VI' web 2nd bending waves. The yellow boxes show the close-up of the results within 2 kHz to better illustrate the difference between the straight and curved rail.

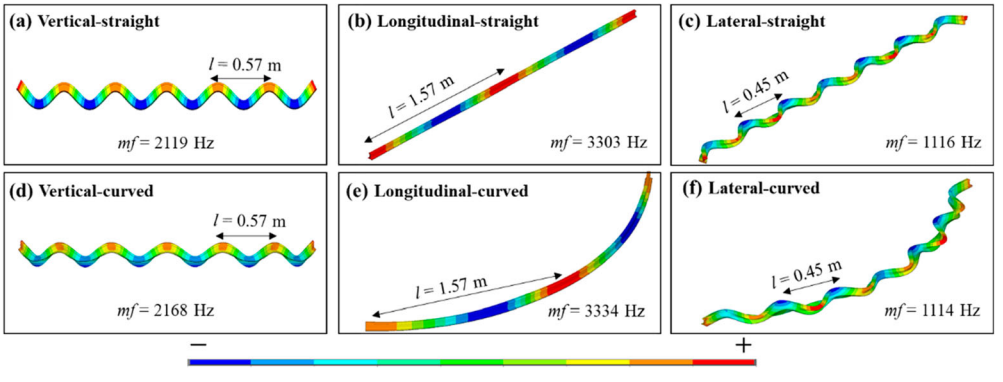

Figure 4. Vibration modes of the straight and curved free rail. (a) Vertical bending mode of the straight rail at 2119 Hz with the wavelength of 0.57 m; (b) longitudinal compression mode of the straight rail at 3304 Hz with the wavelength of 1.57 m; (c) lateral bending mode of the straight rail at 1116 Hz with the wavelength of 0.45 m; (d) vertical bending mode of the curved rail at 2168 Hz with the wavelength of 0.57 m; (e) longitudinal compression mode of the curved rail at 3334 Hz with the wavelength of 1.57 m; (f) lateral bending mode of the straight rail at 1114 Hz with the wavelength of 0.45 m. In this figure, *mf* refers to mode frequency in short from the modal analysis, and the *l* the wavelength of the mode shape.

3.2. Validation of 3D track dynamics by hammer tests

The track parameters, including the stiffness and damping of the fastenings and rubber pads, are derived by fitting the simulated accelerances to the measured ones from hammer

tests. Figure 5 shows the closest fit of the simulation to the measurement in three directions up to 10 kHz. It can be seen that the simulated track dynamics with the straight and curved track almost overlap completely with each other in three directions, further confirming their dynamic similarity. Hereinafter, the results of the straight track are present for ease of analysis and description in the global Cartesian coordinate system. The major characteristic frequencies and their corresponding vibration modes of the track are also identified employing a modal analysis and listed in Table 2.

Figure 5a compares the simulated and measured vertical accelerances. The overall tendency and amplitude of the simulation match the measurement well up to 10 kHz. Further, the simulation result successfully reproduces the six major characteristic frequencies (notated by T_{1z}, T_{2z},… ,T_{6z}) in the measurement. The modal analysis result in Figure 6a shows that T_{1z} at 410 Hz corresponds to the vertical resonance mode of the full track, in which rail and sleeper in-phase vibrate vertically on the elasticity of the rubber pads (ballast) [58]. Following the cutting-on frequency of T_{1z}, there is a series of harmonics of rail vertical bending modes/waves [29,59]. T_{2z} at 610 Hz is one of them with a wavelength (l) of 1.05 m, see the mode shape in Figure 6b, as well as another minor peak at 730 Hz (see Figure 5a). Figure 6c depicts that T_{3z} at 1100 Hz corresponds to the resonance mode of the 1st sleeper bending [52], in which rail vibrates in-phase with the sleeper at rail seats where the sleeper vertically bends. The minor peaks following T_{3z} are also the harmonic

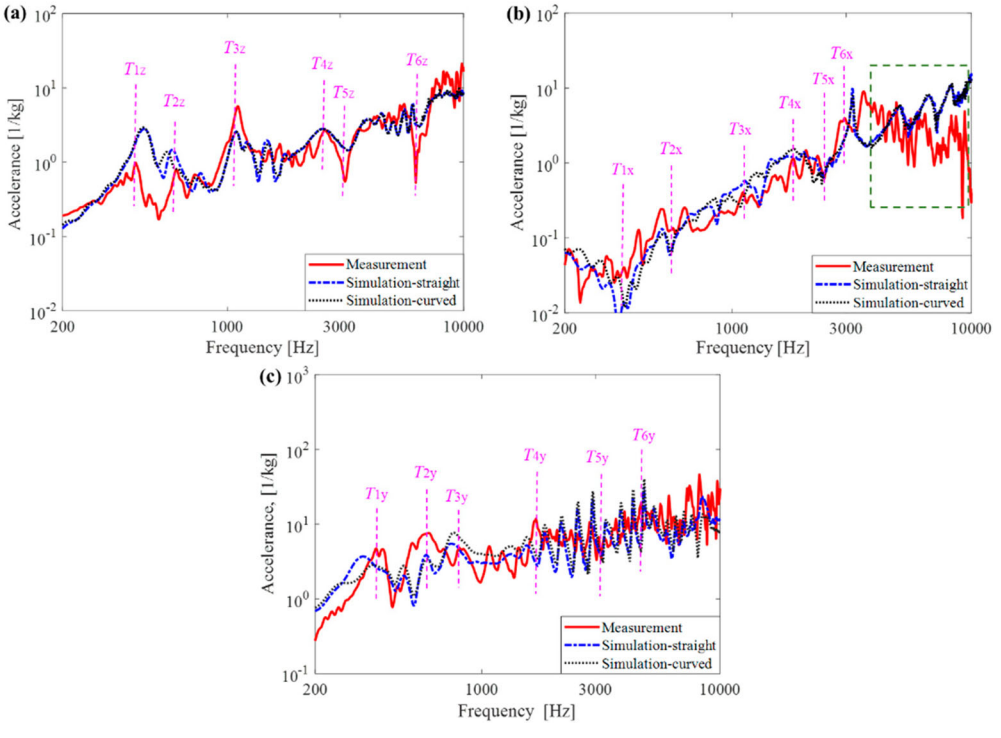

Figure 5. Comparison between simulated and measured track accelerances in the (a) vertical, (b) longitudinal, and (c) lateral directions. The dashed pink lines and corresponding notations (T_{ix}, T_{iy}, T_{iz}) indicate the characteristic frequencies of the track in three directions. The green dashed box in (b) marks the unreliable frequency range of the longitudinal hammer test using the self-made clamp.

Table 2. Comparison of track vibration modes between simulations and measurement.

Notations	Frequency [Hz] (Measurement/Simulation)	Track eigenmodes
T_{1z}	410/440	Full track vertical resonance mode at 437 Hz
T_{2z}	610/590	Rail vertical bending mode at 583 Hz
T_{3z}	1100/1095	Sleeper 1st vertical bending mode at 1148 Hz
T_{4z}	2580/2550	Rail vertical resonance mode at 2479 Hz
T_{5z}	3150/3190	Rail vertical bending mode at 3128 Hz
T_{6z}	6270/6320	Vertical pinned-pinned resonance mode at 6280
T_{1x}	340/335	Sleeper in-plane rotation mode at 330 Hz
T_{2x}	565/550	Sleeper longitudinal translation mode at 597 Hz
T_{3x}	1110/1130	Rail longitudinal resonance mode at 1173 Hz
T_{4x}	1800/1835	Rail longitudinal compression mode at 1943Hz
T_{5x}	2615/2610	Rail longitudinal compression mode at 2691 Hz
T_{6x}	2955/3185	Sleeper in-plane bending mode at 3213 Hz
T_{1y}	360/320	Full track lateral resonance mode at 330 Hz
T_{2y}	600/590	Rail lateral torsion mode at 597 Hz
T_{3y}	800/760	Rail lateral torsion mode at 733 Hz
T_{4y}	1700/1830	Rail lateral bending mode at 1809Hz
T_{5y}	3170/3175	Lateral pinned-pinned resonance at 3159 Hz
T_{6y}	4670/4780	Rail lateral bending mode at 4846 Hz

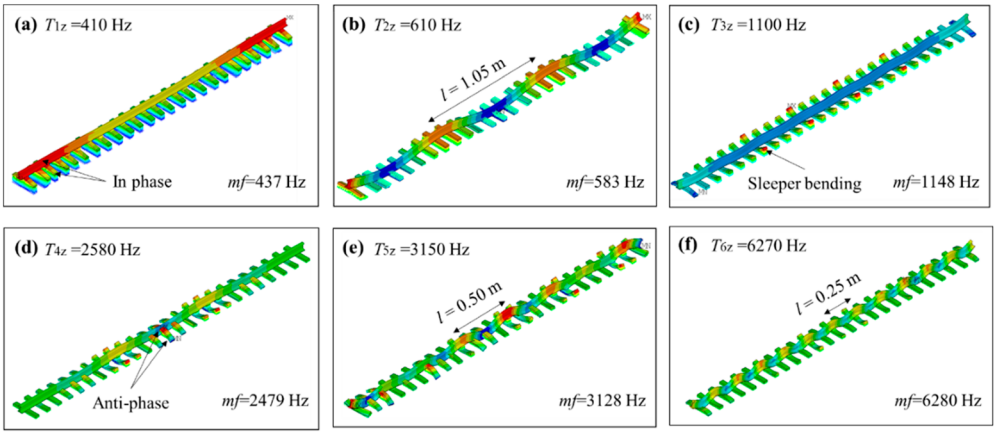

Figure 6. Mode shapes corresponding to the characteristic frequencies of the vertical accelerance. (a) Full track vertical resonance mode at T_{1z}; (b) rail vertical bending mode at T_{2z}; (c) sleeper 1st vertical bending at T_{3z}; (d) rail vertical resonance mode at T_{4z}; (e) rail vertical bending mode at T_{5z}; (f) vertical pinned-pinned resonance mode at T_{6z}. The peak frequency T_{iz} is obtained from the measured accelerance.

bending modes with the cutting-on frequency of T_{3z}. Figure 6d shows that the rail vibrates in anti-phase with the sleeper on the elasticity of rail pads at T_{4z} of 2580 Hz, corresponding to rail vertical resonance mode. T_{5z} at 3150 Hz and T_{6z} at 6270 Hz are two harmonic bending modes after the cutting-on frequency of T_{4z} with wavelengths of four (see Figure 6e) and two (see Figure 6f) sleeper spans, respectively. The latter is also known as vertical pinned-pinned resonance mode. The similarity of these characteristic modes to the field ones will be discussed in Section 5.3.

It is noted from Figure 5a that the simulation overestimates the vertical accelerance between 400 and 600 Hz where sleepers and their constraints play an important role in the track vibration. In the V-Track, the sleeper is fixed by bolts on the plywood with a

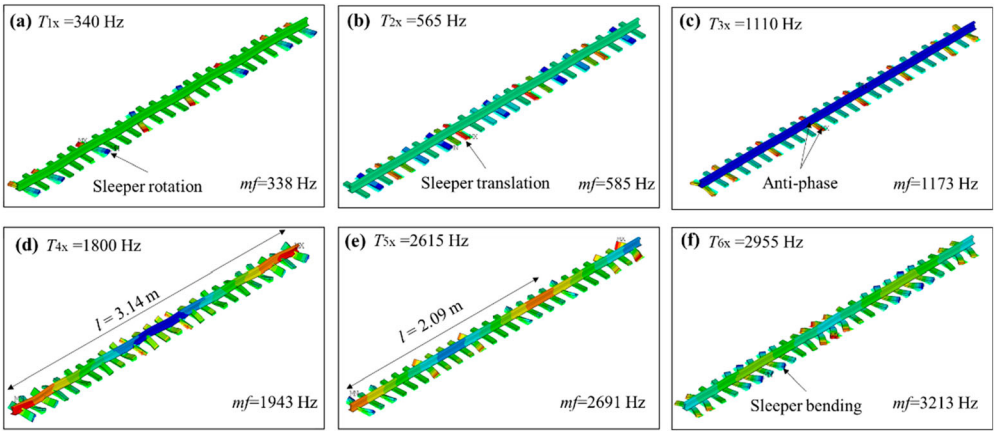

Figure 7. Mode shapes corresponding to the characteristic frequencies of the longitudinal accelerance. (a) Sleeper in-plane rotation mode at T_{1x}; (b) sleeper longitudinal translation mode at T_{2x}; (c) rail longitudinal resonance mode at T_{3x}; (d) rail longitudinal compression mode at T_{4x}; (e) rail longitudinal compression mode at T_{5x}; (f) sleeper in-plane bending mode at T_{6x}. The peak frequency T_{ix} is obtained from the measured accelerance.

rubber pad in between, see Figure 1b. In the simulation, the sleeper bolts are not directly modelled but indirectly considered by compensating it in the stiffness of the fastening and rubber pad, probably underestimating their constraints and thus causing larger vibration level than reality. Besides, the fastening and ballast elasticity are simplified into the linear spring-damper elements instead of a more accurate solid model [45] to save computation cost, which may contribute to the deviation between the simulation and measurement.

Figure 5b compares the simulated and measured longitudinal accelerance. Good agreement between the simulation and the measurement has been achieved up to about 3 kHz in terms of the overall tendencies and vibration amplitude. Considerable differences are observed at frequencies higher than 3 kHz, where the measurement result is not reliable because the self-made clamp (Figure 1c) cannot effectively transfer the hammer excitation to the rail at high frequency. Six longitudinal characteristic modes (notated by T_{1x}, $T_{2x}, \ldots T_{6x}$ in Figure 5b) are identified in both the simulation and measurement, as shown in Figure 7 and Table 2. Among them, T_{1x} at 340 Hz and T_{2x} at 565 Hz are anti-resonance modes, corresponding to the sleeper in-plane (longitudinal-lateral plane) rotation and longitudinal translation modes, respectively, as shown in Figure 7a and b. Figure 7c shows that T_{3x} at 1110 Hz correspond to the rail longitudinal resonance mode, in which the rail moves in anti-phase with sleepers on the longitudinal stiffness of fastenings. T_{4x} at 1800Hz and T_{5x} at 2615 Hz are two harmonic longitudinal compression modes after the cutting-on frequency of T_{3x} with wavelengths of 3.14 m (see Figure 7d) and 2.09 m (see Figure 7e), respectively. Figure 7f shows that at T_{6x} of 3213 Hz, the rail is in compression/rarefaction vibration while sleepers bend in the longitudinal-lateral plane.

The closest fit of the simulated to the measured lateral accelerance is shown in Figure 5c. The overall tendency of the simulation agrees with the measurement up to 10 kHz. Some characteristic frequencies and their corresponding modes are also derived, as summarised in Figure 8 and Table 2, notated as T_{1y}, $T_{2y}, \ldots T_{6y}$. Figure 8a shows that T_{1y} at 360 Hz

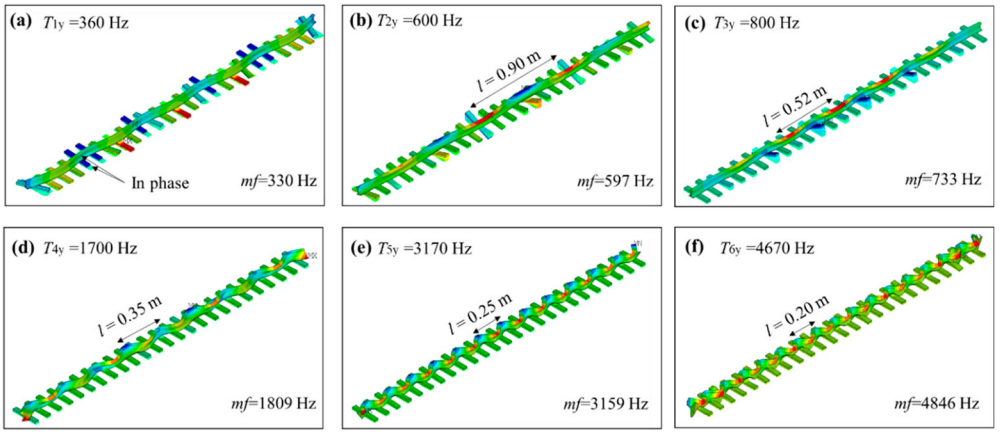

Figure 8. Mode shapes corresponding to the characteristic frequencies of the lateral accelerance. (a) Full track lateral resonance mode at T_{1y}; (b) rail lateral torsion mode at T_{2y}; (c) rail lateral torsion mode at T_{3y}; (d) rail lateral bending mode at T_{4y}; (e) lateral pinned-pinned resonance mode at T_{5y}; (f) rail lateral bending mode at T_{6y}. The peak frequency T_{iy} is obtained from the measured accelerance.

corresponds to full track resonance mode in the lateral direction where the rail and sleepers vibrate in-phase on the lateral stiffness of the rubber pads (ballast). Figure 8b and c show that T_{2y} at 600 Hz and T_{3y} at 800 Hz are two rail lateral torsion modes with the wavelength of 0.90 and 0.52 m, respectively. Figure 8d,e,f show that T_{4y} at 1700Hz, T_{5y} at 3170 Hz and T_{6y} at 4670 Hz correspond to rail lateral bending modes with the wavelength of 0.35, 0.25 and 0.20 m, respectively. Among them, T_{5y} at 3170 Hz is the lateral pinned-pinned resonance mode whose wavelength is twice the sleeper span.

Overall, good agreement has been achieved between the simulated and measured track accelerances in three directions in terms of overall tendency, amplitude and characteristic frequencies, indicating that the proposed model can accurately simulate track dynamic behaviours in the high-frequency range. Meanwhile, the vibration characteristics of the curved rail in the V-Track are approximately equivalent to those of the straight rail in the high-frequency range under the fastening constraints, which provides a basis to achieve dynamic similarity between the V-Track ring track and field tracks and further the wheel-rail interaction.

4. Comprehensive validation of wheel-rail dynamic interaction responses

In this section, the simulated wheel-rail dynamic responses including rail vibrations, wheel-rail contact forces and wheel vibrations, are comprehensively compared with measurement results. Besides, the characteristic frequencies of the wheel-rail dynamic interaction are identified.

4.1. Validation of rail vibrations

Figure 9 compares the simulated and measured rail accelerations in the frequency domain up to 10 kHz in the vertical, longitudinal and lateral directions. These signals are taken

within one sleeper span, half before and after the 75th sleeper, and processed by synchrosqueezed wavelet transform [60]. It can be seen from Figure 9a that the overall tendency and amplitude of the simulated vertical rail acceleration matches the measurement well up to 10 kHz. The vertical rail vibration energy mainly concentrates on six characteristic frequencies, indicated by f_{iz} (i = 1, 2, … , 6) in Figure 9a. They correspond to the eigenmodes of the vehicle-track system, as listed in Table 3, which will be further analysed in Section 5.2. The simulation successfully reproduces them with similar magnitudes to the measurement despite some frequency shift at f_{3z}.

Figure 9b shows that good agreement has been achieved between the simulated and measured longitudinal rail accelerations with respect to the overall trend within 10 kHz and seven characteristic frequencies (notated by f_{ix}, i = 1,2, … ,7). Magnitude deviations are observed at some frequencies, i.e. f_{3x} and f_{5x}. Based on the peak sharpness in Figure 9b, it seems that the damping of the simulation is relatively smaller compared to the measurement at lower frequencies (i.e. f_{1x} and f_{3x}), causing sharper peaks and magnitude overestimation, while that is larger at higher frequencies (i.e. f_{5x}), causing a blunter peak and magnitude underestimation. A non-linear damping parameter instead of the linear one in the current model will be considered in future research to narrow the gap.

Figure 9c compares the simulated and measured lateral rail accelerations, and their average vibration levels generally match each other. The simulation basically captures the main

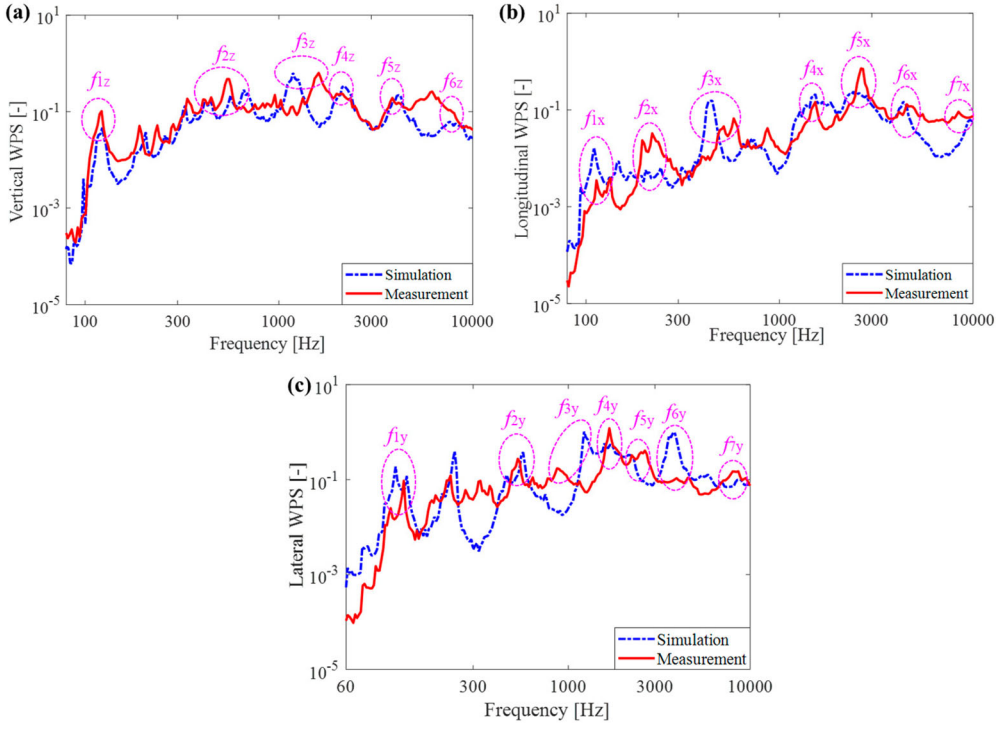

Figure 9. Comparison of simulated and measured rail accelerations in the frequency domain in the (a) vertical, (b) longitudinal, and (c) lateral directions. The dashed pink ovals and corresponding notations (f_{ix}, f_{iy}, f_{iz}) indicate the characteristic frequencies of the vehicle-track dynamic interaction in three directions.

Table 3. Characteristic frequencies and their corresponding eigenmodes of vehicle-track system.

Notations	Frequency [Hz]	Eigenmodes of vehicle-track system
f_{1z}	100–130	P2 resonance mode
f_{2z}	450–600	Rail vertical bending mode at 583 Hz (T_{2z})
f_{3z}	1000–1200	Sleeper 1st vertical bending mode at 1148 Hz (T_{3z})
f_{4z}	1900–2300	Rail vertical resonance mode at 2479 Hz (T_{4z})
f_{5z}	4000–4500	Zero nodal circle and two nodal diameters at 4143 Hz
f_{6z}	8500–8700	One nodal circle and zero nodal diameters at 8127 Hz
f_{1x}	100–130	P2 resonance mode, coupling from f_{1z}
f_{2x}	220–260	Sleeper in-plane rotation mode at 330 Hz (T_{1x})
f_{3x}	450–600	Sleeper longitudinal translation mode at 597 Hz (T_{2x})
f_{4x}	1200–1500	Wheel axle bending mode at 1235 Hz
f_{5x}	2300–2700	Rail longitudinal compression mode at 2691 Hz (T_{5x})
f_{6x}	4300–4500	Zero nodal circle and two nodal diameters at 4143 Hz
f_{7x}	8500–8700	One nodal circle and zero nodal diameters at 8127 Hz
f_{1y}	100–130	P2 resonance mode, coupling from f_{1z}
f_{2y}	450–600	Rail lateral torsion mode at 597 Hz (T_{2y})
f_{3y}	1000–1200	Wheel axle bending mode at 1235 Hz
f_{4y}	1600–1800	Rail lateral bending mode at 1809Hz (T_{4y})
f_{5y}	2100–2500	Zero nodal circle and one nodal diameters at 2337 Hz
f_{6y}	3900–4300	Zero nodal circle and two nodal diameters at 4143 Hz
f_{7y}	8500–8700	One nodal circle and zero nodal diameters at 8127 Hz

frequency contents of the measurement, notated by $f_{1y}, f_{2y} \ldots, f_{7y}$, with close magnitudes at $f_{1y}, f_{2y}, f_{5y}, f_{7y}$. Compared to the vertical and longitudinal directions, the relatively large difference between the lateral simulation and measurement is possibly caused by that the ring rails are not purely circular in reality, leading to varying AoA and lateral wheel-rail dynamic interaction in the measurement.

Overall, the good agreement between the simulation and measurement in the vertical and longitudinal directions and reasonable agreement in the lateral direction indicate that the proposed 3D FE model can accurately simulate vehicle-track high-frequency interaction in three directions.

4.2. Validation of wheel-rail contact force

Figure 10 compared the simulated and measured wheel-rail contact force in three directions. It can be seen from Figure 10a that the simulation successfully reproduces the five characteristic frequencies of the vertical force, as marked by dashed pink ovals. The simulated magnitude of the vertical force is comparable to that from the measurement within 1.2 kHz, but considerably larger at higher frequencies. The reason is that the current dynamometer is designed to measure the wheel-rail contact force without compensation for the inertia force of the wheel assembly [48], and thus may not accurately measure the dynamic magnitude. Nevertheless, the results in Figure 10a indicate that the dynamometer can indeed capture the dynamic effect of the vehicle-track interaction and the characteristic frequencies. Meantime, it can be concluded that the vertical inertia force of the wheel assembly is relatively small at lower frequencies than 1.2 kHz, but become much more significant above 1.2 kHz. Similarly to the vertical direction, the longitudinal and lateral simulations also capture the characteristic frequencies of the measured longitudinal and lateral forces and have much larger magnitudes at higher frequencies than 1.2 kHz, as shown in Figure 10b and c.

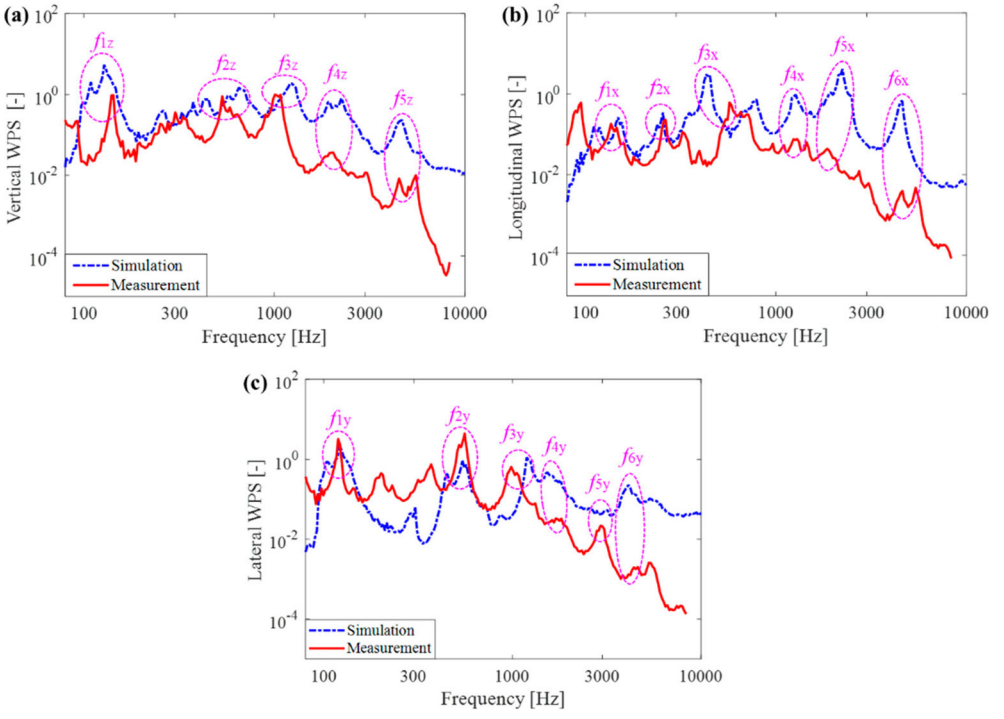

Figure 10. Comparison of simulated and measured contact forces in the (a) vertical, (b) longitudinal, and (c) lateral directions. The dashed pink ovals and corresponding notations (f_{ix}, f_{iy}, f_{iz}) indicate the characteristic frequencies of the vehicle-track dynamic interaction in three directions.

Overall, reasonable agreement is achieved between simulation and measurement in terms of the characteristic frequencies of the wheel-rail contact forces and the magnitudes below 1.2 kHz. Besides, the results indicate the dynamometer can capture the high-frequency dynamic behaviours of the V-Track, despite an underestimation of the magnitude above 1.2 kHz where the wheel inertia force plays an important role.

4.3. Validation of wheel vibrations

Figure 11 compares the simulated wheel accelerations with measured ABA in three directions. It can be seen from Figure 10a that the simulated vertical wheel acceleration reproduces the first four characteristic frequencies of the measured ABA. The characteristic frequencies of f_{5z} and f_{6z} are only observed in the simulation. Besides, the simulated magnitude is comparable to that of measurement below 1 kHz, but considerably larger at higher frequencies. The differences between the simulation and measurement are probably caused by the axle box of the wheel assembly which has a significantly larger volume and mass compared to the wheel (see Figure 1b). Therefore, the high-frequency wheel vibration cannot effectively excite the heavy axle box and thus cannot be captured by the accelerometers on it, leading to the mismatch of the characteristic frequencies f_{5z} and f_{6z} and magnitudes above 1 kHz. Similar results are found in the longitudinal (see Figure 11b) and lateral (see Figure 11c) directions; only the first four and five characteristic frequencies are captured in the ABA measurement, and the simulation signals are much stronger

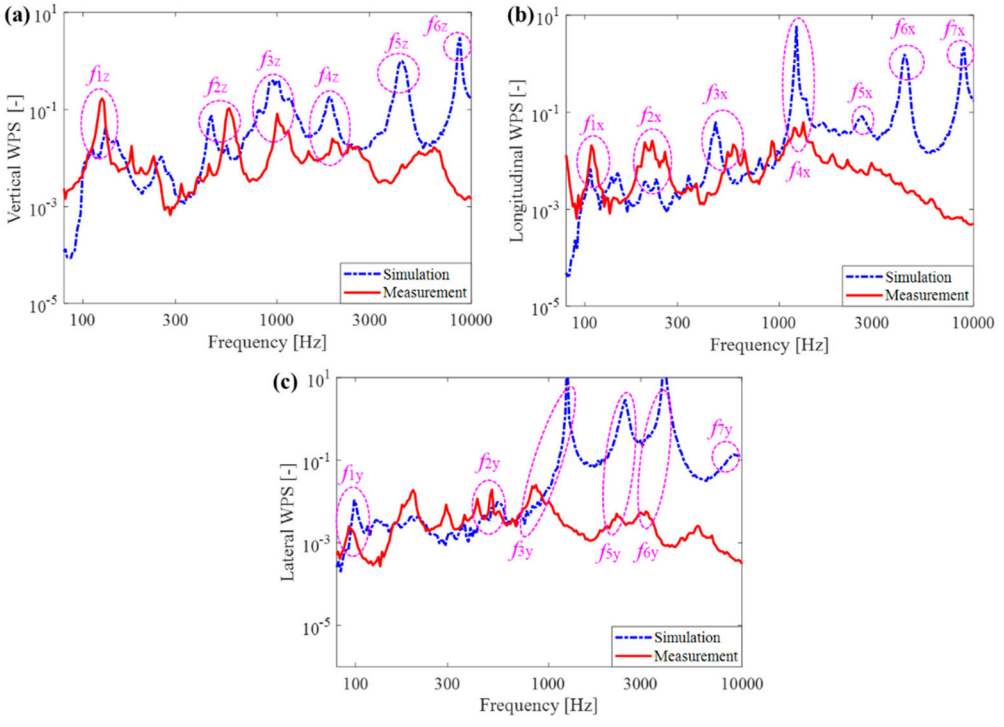

Figure 11. Comparison of simulated wheel accelerations and measured ABA in the (a) vertical, (b) longitudinal, and (c) lateral directions. The dashed pink ovals and corresponding notations (f_{ix}, f_{iy}, f_{iz}) indicate the characteristic frequencies of the vehicle-track dynamic interaction in three directions.

than those of measurement at higher frequencies than 1 kHz. In the field, the axle box is relatively small compared to the wheel and thus ABA can be more comparable to the wheel vibrations [43]. Besides, the wheel damping may be insufficient in the simulation, leading to the strong wheel resonance at higher frequencies, which is better suppressed in reality through, e.g. the friction between the wheel, axle box and primary suspension. In future work, more realistic wheel constraints will be considered in the FE model.

In summary, the pass-by rail vibrations have achieved the best agreement between the simulation and measurement owing to the careful treatment and accurate simulation of 3D track dynamics. The wheel-rail contact force measurement underestimate the force magnitude above 1.2 kHz without compensation for the inertia force of the wheel assembly, and the ABA measurement cannot accurately reflect the wheel vibration amplitude at frequencies higher than 1.0 kHz because of the axle box bulkiness. Nevertheless, they can both capture the high-frequency dynamic behaviours of the V-Track in terms of characteristic frequencies.

5. Discussions

This section discusses the relationship between contact forces and vibrations of the vehicle-track system (Section 5.1), the correlations between vibration characteristics and

eigenmodes (Section 5.2), and dynamic similarity between the V-Track test rig and the real vehicle-track system (Section 5.3).

5.1. The relationship between contact forces and vibrations of the vehicle-track system

Figure 12 shows the simulated contact forces together with the rail and wheel accelerations in three directions. It can be seen that the contact forces have generally the same characteristic frequencies as the rail and wheel accelerations except for the f_{6z}, f_{7x} and f_{7y}. The absence of these higher-frequency components above 5 kHz in the contact forces is probably related to the contact filter effect that the wavelength roughness shorter than the contact patch size cannot effectively excite the wheel-rail contact resonance [61,62]. The simulation results in [63] also indicate that the employed 3D FE model inherently includes the contact filter effect that becomes important when the size of a defect is similar to or less than the contact patch size. Besides, it is found that the average magnitudes of contact force shows a drop above about 2 kHz (see the dashed green lines), corresponding to a wavelength shorter than about 1.8 mm with the running speed of 13 km/h. This size is

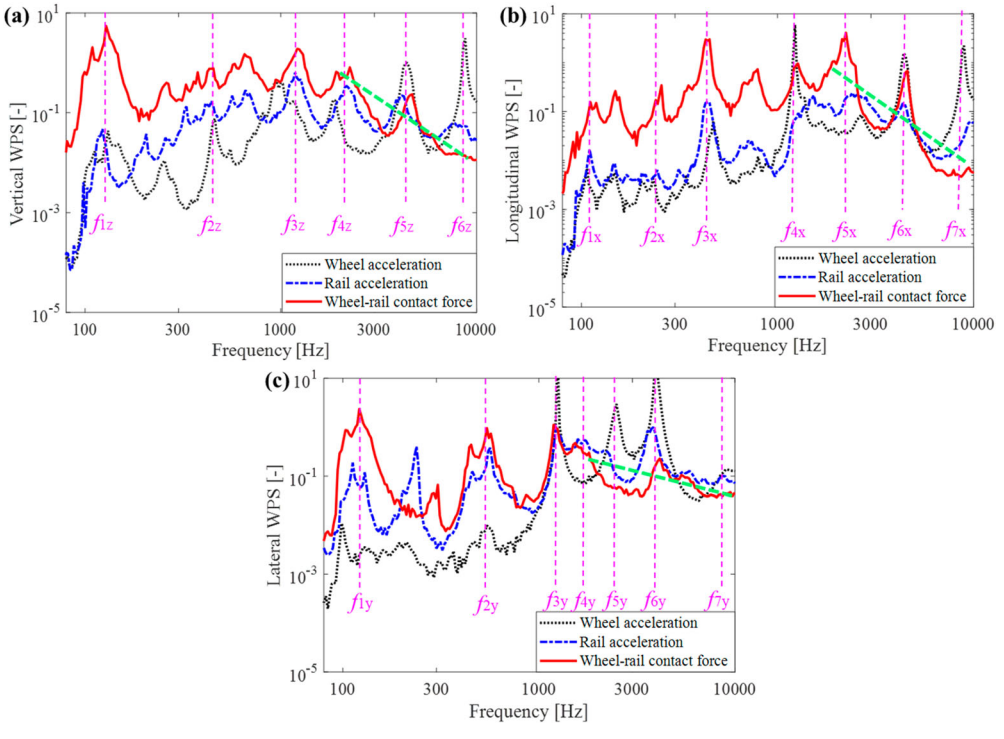

Figure 12. The relationship between contact forces and vibration responses of the vehicle-track system in the (a) vertical, (b) longitudinal, and (c) lateral directions. The dashed pink ovals and corresponding notations (f_{ix}, f_{iy}, f_{iz}) indicate the characteristic frequencies of the vehicle-track dynamic interaction in three directions. The green dashed lines show the downward trend of the contact forces due to the contact filter effect.

quite close to the contact patch length of about 2 mm in the rolling direction, confirming the effect of the contact filter.

It can be seen from Figure 12a that the peak at f_{1z} of the vertical contact force is predominant. It corresponds to the so-called P2 resonance mode in which the wheel and the rail vibrate together on the overall track stiffness [64]. This can be confirmed by the fact that at f_{1z}, the wheel and the rail have almost the same vibration magnitude. We also observe similar characteristic frequencies in the longitudinal (f_{1x} in Figure 12b) and lateral (f_{1y} in Figure 12c) direction, which should be coupled from the vertical contact force through friction.

In most situations, the rail accelerations are larger than the wheel accelerations in three directions in 0–10 kHz although the differences become relatively smaller with increasing frequencies. The overall tendency of rail accelerations correlates well to that of the contact forces. These results indicate the rail vibrations basically dominate the wheel-rail dynamic contact in the frequency range of 0–10 kHz, while the wheel vibrations play an increasingly important role at higher frequencies. This agrees with the results in Section 4.2 that the wheel inertia force plays an important role above 1.2 kHz. Meanwhile, it is noted that at some characteristic frequencies, such as f_{5z}, f_{4x}, and f_{6y}, the wheel acceleration is much larger than the rail acceleration and thus more dominant for the contact force peaks. The reason is that these characteristic frequencies are correlated to the eigenmodes of the wheel, which will be discussed in more detail in section 5.2.

5.2. The correlations between vibration characteristics and eigenmodes of vehicle-track system

In this section, the characteristic frequencies of the vehicle-track dynamic interaction are correlated to the eigenmodes of vehicle-track system, as listed in Table 3. In the vertical direction, f_{1z} corresponds to the P2 resonance mode, as explained in Section 5.1. Combining the vertical track dynamics in Figure 5a with the characteristic frequencies in Figure 12a, it can be found that f_{2z}, f_{3z}, f_{4z} are correlated to the rail vertical bending mode at 583 Hz (T_{2z}), sleeper 1st vertical bending mode at 1148 Hz (T_{3z}), rail vertical resonance mode at 2479 Hz (T_{4z}), respectively. At f_{5z} and f_{6z} the wheel shows strong resonance vibration with considerably large magnitude, and the modal analysis results indicate that these characteristic frequencies correspond to two wheel eigenmodes with zero nodal circle and two nodal diameters at 4143 Hz (Figure 13c) and one nodal circle and zero nodal diameters at 8127 Hz (Figure 13d).

In the longitudinal direction, f_{1x} corresponds to the P2 resonance mode that couples with the vertical one through friction. By analysing the track accelerance in Figure 5b and characteristic frequencies in Figure 12b, it is observed that f_{2x}, f_{3x}, f_{5x} are correlated to sleeper in-plane rotation mode at 330 Hz (T_{1x}), sleeper longitudinal translation mode at 597 Hz (T_{2x}), and rail longitudinal compression mode at 2691 Hz (T_{5x}), respectively. At f_{4x}, f_{6x}, and f_{7x}, the wheel vibration energy is significantly larger than that of the rail, caused by the resonance at three wheel eigenmodes, as shown in Figure 13a,c and d. In the lateral direction, f_{1y} corresponds to the P2 resonance mode as explained above, f_{2y} and f_{4y} are correlated to rail lateral torsion mode at 597 Hz (T_{2y}), rail lateral bending mode at 1809Hz (T_{4y}), respectively. The large wheel vibration magnitudes at f_{3y}, f_{5y}, f_{6y} and f_{7y} indicate that they are induced by four wheel eigenmodes, wheel axle bending mode (Figure 13a),

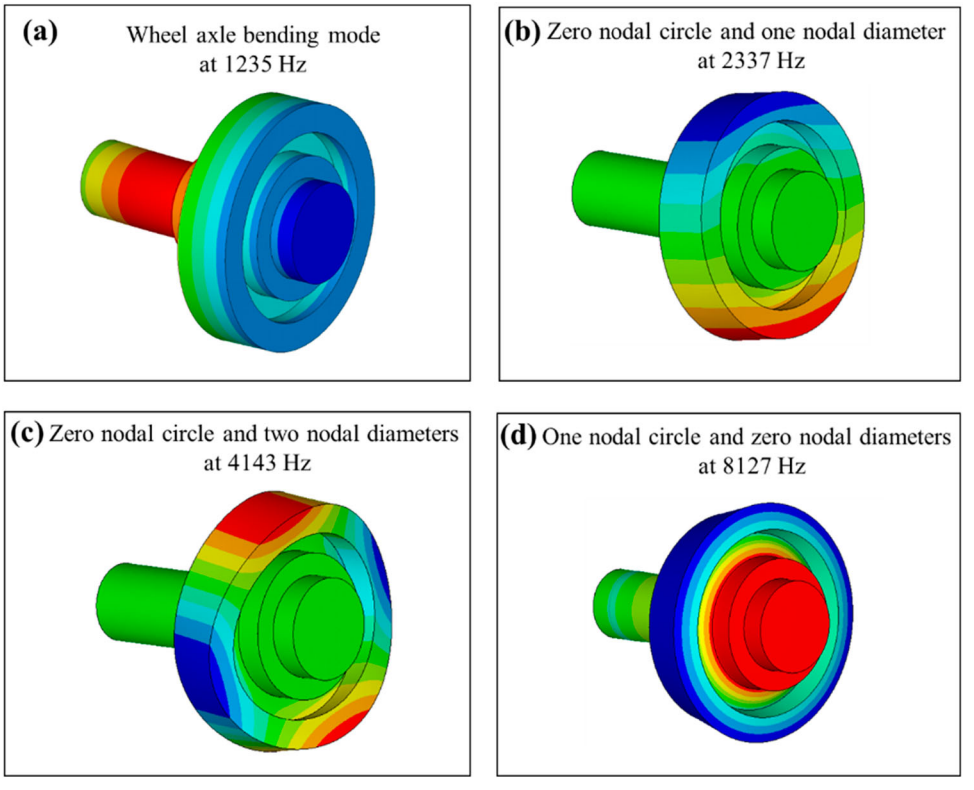

Figure 13. Four wheel eigenmodes correlated to the vehicle-track dynamic interaction. (a) Wheel axle bending mode at 1235 Hz; (b) zero nodal circle and one nodal diameter at 2337 Hz; (c) zero nodal circle and two nodal diameters at 4671 Hz; (d) one nodal circle and zero nodal diameters at 8127 Hz.

zero nodal circle and one nodal diameter (Figure 13b), zero nodal circle and two nodal diameters (Figure 13c), and. one nodal circle and zero nodal diameters (Figure 13d).

In summary, the characteristic frequencies of vehicle-track dynamic interaction are correlated to the eignemodes of the vehicle-track system in three directions, including the P2 resonance mode, track and wheel eigenmodes. In the tangential (i.e. longitudinal and lateral) direction, the characteristic frequencies may be caused by the coupling with the normal (vertical in this work) direction through wheel-rail friction. Besides, it can be seen that the lateral vehicle-track dynamic interaction excites the wheel eigenmodes the most easily, compared to the longitudinal and vertical direction.

5.3. The wheel-rail dynamic interaction under the large creep force

In the previous tests and FE simulations, the loading conditions and wheel-rail profiles of the V-Track were designed to simulate the 3D wheel-rail dynamic interactions on the tangent track where the longitudinal and lateral creep forces are relatively small. In this subsection, some preliminary results have been presented to demonstrate the capacity of the proposed 3D FE model in simulating wheel-rail dynamic interaction under large longitudinal and lateral creep forces.

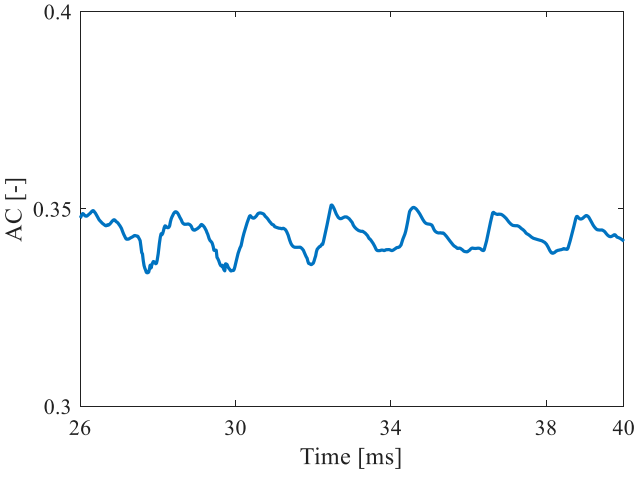

Figure 14. The simulated wheel-rail stick-slip with an AoA of 28 mrad. 'AC' refers to the adhesion coefficient in short.

The large longitudinal creep force can be readily considered in the simulation by applying a large braking or traction torque to the wheel axle in the FE model. The large longitudinal force can cause high temperatures at the wheel-rail interface that can be measured through thermal tests [65]. The proposed FE model successfully predicted the temperature field on the rail surface under full-slip wheel-rail rolling contact [65], indicating that it can properly simulate the wheel-rail dynamic interaction under a large longitudinal creep force.

The large lateral creep force can be simulated in the FE model with a large AoA. The wheel-rail stick-slip was successfully reproduced using the FE model with a large AoA of 28 mrad, as shown in Figure 14, agreeing with the observations in the V-Track tests [66]. The stick-slip phenomenon has also been widely reported in the field curved track [67]. This result indicates that the proposed FE model is capable of properly simulating wheel-rail lateral dynamic interaction under a large lateral creep force. Besides, to better simulate wheel-rail lateral interaction, a conical wheel and the corresponding rail profile can be designed and applied to the V-Track test rig and the FE model. The design method of the wheel-rail profile in the V-Track is introduced in detail in [50].

5.4. The dynamic similarity between the V-Track and real vehicle-track system

It is reported in [47] that the V-Track test rig intends to remedy the lack of dynamic similarity between the actual railway and the existing laboratory testing capability. To quantitatively examine this, the dynamic behaviours of the V-Track are compared with those of the real railway system in terms of the characteristic modes, as listed in Table 4. The current V-Track configuration is approximately 1/5 scale of the real system, which will be considered in the comparison according to the similarity law [47]. The results of the real railway are referred to the literature that studied the Dutch railway on which the parameter design of the V-Track is based. It should be noted that the nonlinearities of the wheel-rail dynamic system may influence the scale factors obtained by the similarity law, which are not considered in the current work.

Table 4. Comparison of vehicle-track dynamics between the V-Track and real railway system.

	Modes	V-Track (Hz)	1/5 scale of V-Track (Hz)	Real system (Hz)
Track dynamics	Full track vertical resonance	437	87	90 [68]
	Sleeper 1st vertical bending	1148	230	197 [52]
	Rail vertical resonance	2479	496	715 [52]
	Vertical pinned-pinned resonance	6280	1256	1250 [52]
	Lateral pinned-pinned resonance	3159	632	600 [69]
Wheel dynamics	Wheel mode with zero nodal circle and two nodal diameters	4143	934	407 [70]
	Wheel mode with one nodal circle and zero nodal diameters	8127	1625	1522 [70]
Vehicle-track interaction	P2 resonance	100–130	20–26	38 [68]

Good similarity of track dynamics is achieved between the V-Track and the real system in terms of the full track vertical resonance, sleeper 1st vertical bending, vertical and lateral pinned-pinned resonances. The rail vertical resonance of the V-Track (after scaling) is smaller than that of the real track, which is caused by the absent fastening clips at some sleepers. The wheel dynamics of these two systems is also comparable if we look at the wheel mode with one nodal circle and zero nodal diameters. A relatively large deviation is observed at the wheel mode with zero nodal circle and two nodal diameters, which is due to the imperfect scale of the wheel profile in the V-Track for ease of manufacturing [48]. The P2 resonance of the V-Track is slightly smaller than that of the real system, probably because of the additional unsprung mass from the guiding block (see Figure 1b). Additionally, the results in Section 3 indicate that the vibration characteristics of the curved rail in the V-Track are approximately equivalent to those of the straight rail in the relatively high-frequency range under fastening constraints.

Overall, the V-Track has achieved generally good dynamic similarity to the real vehicle-track system. The proposed 3D FE model is capable of reproducing the wheel-rail high-frequency interaction of the V-Track, and thus can be employed to gain insights into the actual vehicle-track interaction. Meanwhile, the validity of this model could be extended to the 3D FE modelling of the real vehicle-track system.

6. Conclusions

This work comprehensively validates the FE modelling of vehicle-track high-frequency interaction using a downscale V-Track test rig. A 3D FE model of the V-Track is developed that includes the track elasticity in not only the vertical but also the longitudinal and lateral directions. The 3D track dynamics of the curved and straight tracks are compared and validated against those from hammer tests, and the major vibration modes of the track are analysed employing a modal analysis. Afterwards, the simulated vehicle-track dynamic interaction responses including pass-by rail vibrations, wheel-rail contact forces and wheel vibrations, are comprehensively compared with measurement results in three dimensions within 10 kHz. Their characteristic frequencies are identified and correlated to the eigenmodes of the vehicle-track system. In addition, the dynamic similarity between the V-Track test rig and the real railway system is quantitatively evaluated. The main findings are summarised as follows.

The proposed 3D FE model is capable of comprehensively and accurately simulating the track dynamics and the vehicle-track dynamic interaction of the V-Track up to 10 kHz in three dimensions. The simulation results also indicate that the dynamic behaviours of the curved rail in the V-Track are approximately equivalent to those of the straight rail in the high frequency range under fastening constraints.

By analysing the relationship between contact forces and vibrations of the vehicle-track system, it is concluded that rail vibrations are generally dominant for the wheel-rail dynamic contact in the frequency range of 0–10 kHz, while the wheel vibrations play an increasingly important role at higher frequencies and decisive near the wheel eigenmode frequencies. It is also found that the 3D FE model inherently includes the contact filter effect in three dimensions.

The V-Track test rig overall achieves dynamic similarity to the real vehicle-track system in terms of characteristic frequencies, and better similarity can be obtained by using the rail and wheel geometries better scaled to the field ones. It should be noted that the nonlinearities of the wheel-rail dynamic system may influence the dynamic similarity of the V-Track, which needs to be further studied in future work. The dynamometer and ABA measurement can capture the high-frequency dynamic behaviours of the V-Track, despite an underestimation of the magnitude at higher frequencies than about 1 kHz. The contact force measurement of the dynamometer can be improved at higher frequencies by compensating the wheel inertia force. The simulation accuracy of the 3D FE model can be further improved by considering the nonlinear material properties of railpads and increasing damping to the wheel, which will be performed in future research.

Disclosure statement

No potential conflict of interest was reported by the author(s).

Funding

Parts of the study have been funded from the European Union's Horizon 2020 research and innovation programme in the project In2Track2 under [grant agreement No. 826255] and project In2Track3 under [grant agreement No. 101012456]; European Commission.

References

[1] Grassie SL. Studs and squats: the evolving story. Wear. 2016;366-367:194–199. doi:10.1016/j.wear.2016.03.021

[2] Zhai W, Jin X, Wen Z, et al. Wear problems of high-speed wheel/rail systems: observations, causes, and countermeasures in China. Appl Mech Rev. 2020;72. doi:10.1115/1.4048897

[3] Grassie SL. The corrugation of railway rails: 1. Introduction and mitigation measures. Proc Inst Mech Eng, Part F: J Rail Rapid Transit. 2022;09544097221125626.

[4] Jin X. Research progress of high-speed wheel–rail relationship. Lubricants. 2022;10:248. doi:10.3390/lubricants10100248

[5] Zhang P, Li S, Li Z. Short pitch corrugation mitigation by rail constraint design. Int J Mech Sci. 2022;243:108037.

[6] Correa N, Vadillo E, Santamaria J, et al. A versatile method in the space domain to study short-wave rail undulatory wear caused by rail surface defects. Wear. 2016;352-353:196–208. doi:10.1016/j.wear.2016.02.012

[7] Giannakos K. Modeling the influence of short wavelength defects in a railway track on the dynamic behavior of the non-suspended masses. Mech Syst Signal Process. 2016;68-69:68–83. doi:10.1016/j.ymssp.2015.07.020
[8] Zhao X, Chen G, Lv J, et al. Study on the mechanism for the wheel polygonal wear of high-speed trains in terms of the frictional self-excited vibration theory. Wear. 2019;426-427:1820–1827. doi:10.1016/j.wear.2019.01.020
[9] Li Z, Li S, Zhang P, et al. Mechanism of short pitch rail corrugation: initial excitation and frequency selection for consistent initiation and growth. Int J Rail Transp. 2022;12:1–36.
[10] Yang Y, Ling L, Wang C, et al. Wheel/rail dynamic interaction induced by polygonal wear of locomotive wheels. Veh Syst Dyn. 2022;60:211–235. doi:10.1080/00423114.2020.1807572
[11] Knothe K, Grassie S. Modelling of railway track and vehicle/track interaction at high frequencies. Veh Syst Dyn. 1993;22:209–262. doi:10.1080/00423119308969027
[12] Zhai W, Sun X. A detailed model for investigating vertical interaction between railway vehicle and track. Veh Syst Dyn. 1994;23:603–615. doi:10.1080/00423119308969544
[13] Zhai W, Wang K. Lateral interactions of trains and tracks on small-radius curves: simulation and experiment. Veh Syst Dyn. 2006;44:520–530. doi:10.1080/00423110600875260
[14] Zhai W, Wang K, Cai C. Fundamentals of vehicle–track coupled dynamics. Veh Syst Dyn. 2009;47:1349–1376. doi:10.1080/00423110802621561
[15] Wei K, Wang F, Wang P, et al. Effect of temperature- and frequency-dependent dynamic properties of rail pads on high-speed vehicle–track coupled vibrations. Veh Syst Dyn. 2017;55:351–370. doi:10.1080/00423114.2016.1267371
[16] Xu L, Zhai W. Vehicle–track–tunnel dynamic interaction: a finite/infinite element modelling method. Railway Eng Sci. 2021;29:109–126. doi:10.1007/s40534-021-00238-x
[17] Han Z, Zhu S, Zhai W, et al. Static and dynamic effects of train-track-bridge system subject to environment-induced deformation of long-span railway bridge. Proc Inst Mech Eng, Part F: J Rail Rapid Transit. 2023;237:93–103. doi:10.1177/09544097221095260
[18] Xu L, Zhao Y, Li Z, et al. Three-dimensional vehicle-ballasted track-subgrade interaction: model construction and numerical analysis. Appl Math Model. 2020;86:424–445. doi:10.1016/j.apm.2020.05.007
[19] Thompson D. Wheel-rail noise generation, part IV: contact zone and results. J Sound Vib. 1993;161:447–466. doi:10.1006/jsvi.1993.1085
[20] Wu T, Thompson D. Vibration analysis of railway track with multiple wheels on the rail. J Sound Vib. 2001;239:69–97. doi:10.1006/jsvi.2000.3157
[21] Nielsen JC. High-frequency vertical wheel–rail contact forces—validation of a prediction model by field testing. Wear. 2008;265:1465–1471. doi:10.1016/j.wear.2008.02.038
[22] Jin X, Wen Z, Wang K, et al. Three-dimensional train–track model for study of rail corrugation. J Sound Vib. 2006;293:830–855. doi:10.1016/j.jsv.2005.12.013
[23] Jin X, Wen Z, Zhang W, et al. Numerical simulation of rail corrugation on a curved track. Comput Struct. 2005;83:2052–2065. doi:10.1016/j.compstruc.2005.03.012
[24] Stojanović V, Petković MD, Deng J. Stability of vibrations of a moving railway vehicle along an infinite complex three-part viscoelastic beam/foundation system. Int J Mech Sci. 2018;136:155–168. doi:10.1016/j.ijmecsci.2017.12.024
[25] Xu L, Chen X, Li X, et al. Development of a railway wagon-track interaction model: case studies on excited tracks. Mech Syst Signal Process. 2018;100:877–898. doi:10.1016/j.ymssp.2017.08.008
[26] Escalona JL, Aceituno JF. Multibody simulation of railway vehicles with contact lookup tables. Int J Mech Sci. 2019;155:571–582. doi:10.1016/j.ijmecsci.2018.01.020
[27] Dimitrovová Z. Two-layer model of the railway track: analysis of the critical velocity and instability of two moving proximate masses. Int J Mech Sci. 2022;217:107042. doi:10.1016/j.ijmecsci.2021.107042
[28] Baeza L, Fayos J, Roda A, et al. High frequency railway vehicle-track dynamics through flexible rotating wheelsets. Veh Syst Dyn. 2008;46:647–659. doi:10.1080/00423110701656148

[29] Shen C, Deng X, Wei Z, et al. Comparisons between beam and continuum models for modelling wheel-rail impact at a singular rail surface defect. Int J Mech Sci. 2021;198:106400. doi:10.1016/j.ijmecsci.2021.106400
[30] Knothe K, Groß-Thebing A. Short wavelength rail corrugation and non-steady-state contact mechanics. Veh Syst Dyn. 2008;46:49–66. doi:10.1080/00423110701590180
[31] Srivastava J, Sarkar P, Ranjan V. Contact stress analysis in wheel–rail by Hertzian method and finite element method. J Inst Eng India Ser C. 2014;95:319–325. doi:10.1007/s40032-014-0145-x
[32] Wiedorn J, Daves W, Ossberger U, et al. Simplified explicit finite element model for the impact of a wheel on a crossing – validation and parameter study. Tribol Int. 2017;111:254–264. doi:10.1016/j.triboint.2017.03.023
[33] Mandal NK, Dhanasekar M. Sub-modelling for the ratchetting failure of insulated rail joints. Int J Mech Sci. 2013;75:110–122. doi:10.1016/j.ijmecsci.2013.06.003
[34] Yang Z, Zhang P, Wang L. Wheel-rail impact at an insulated rail joint in an embedded rail system. Eng Struct. 2021;246:113026. doi:10.1016/j.engstruct.2021.113026
[35] Han L, Jing L, Zhao L. Finite element analysis of the wheel–rail impact behavior induced by a wheel flat for high-speed trains: The influence of strain rate. Proc Inst Mech Eng, Part F: J Rail Rapid Transit. 2018;232:990–1004. doi:10.1177/0954409717704790
[36] Wu B, Shang Z, Pan J, et al. Analysis on the formation cause for the high-order wheel polygonization of the high-speed trains based on the finite element method. Veh Syst Dyn. 2023;61:1–18. doi:10.1080/00423114.2022.2035777
[37] Chen G, Zhou Z, Ouyang H-j, et al. A finite element study on rail corrugation based on saturated creep force-induced self-excited vibration of a wheelset–track system. J Sound Vib. 2010;329:4643–4655. doi:10.1016/j.jsv.2010.05.011
[38] Deng X, Li Z, Qian Z, et al. Pre-cracking development of weld-induced squats due to plastic deformation: five-year field monitoring and numerical analysis. Int J Fatigue. 2019;127:431–444. doi:10.1016/j.ijfatigue.2019.06.013
[39] Farjoo M, Daniel W, Bellette P, et al. Field statistical and finite element analysis of rail squats. Eng Fract Mech. 2013;109:117–129. doi:10.1016/j.engfracmech.2013.05.004
[40] Yang Z, Deng X, Li Z. Numerical modeling of dynamic frictional rolling contact with an explicit finite element method. Tribol Int. 2019;129:214–231. doi:10.1016/j.triboint.2018.08.028
[41] Zhao X, Li Z. The solution of frictional wheel–rail rolling contact with a 3D transient finite element model: validation and error analysis. Wear. 2011;271:444–452. doi:10.1016/j.wear.2010.10.007
[42] Toumi M, Chollet H, Yin H. Finite element analysis of the frictional wheel-rail rolling contact using explicit and implicit methods. Wear. 2016;366-367:157–166. doi:10.1016/j.wear.2016.06.008
[43] Molodova M, Li Z, Núñez A, et al. Validation of a finite element model for axle box acceleration at squats in the high frequency range. Comput Struct. 2014;141:84–93. doi:10.1016/j.compstruc.2014.05.005
[44] An B, Wang P, Xu J, et al. Observation and simulation of axle box acceleration in the presence of rail weld in high-speed railway. Appl Sci. 2017;7:1259. doi:10.3390/app7121259
[45] Oregui M, Li Z, Dollevoet R. An investigation into the modeling of railway fastening. Int J Mech Sci. 2015;92:1–11. doi:10.1016/j.ijmecsci.2014.11.019
[46] Zhang P, Li S, Núñez A, et al. Vibration modes and wave propagation of the rail under fastening constraint. Mech Syst Signal Process. 2021;160:107933. doi:10.1016/j.ymssp.2021.107933
[47] Naeimi M, Li Z, Petrov RH, et al. Development of a new downscale setup for wheel-rail contact experiments under impact loading conditions. Exp Tech. 2018;42:1–17. doi:10.1007/s40799-017-0216-z
[48] Zhang P, Moraal J, Li Z. Design, calibration and validation of a wheel-rail contact force measurement system in V-Track. Measurement (Mahwah N J). 2021;175:109105. doi:10.1016/j.measurement.2021.109105
[49] Zhang P, Li Z. Experimental study on the development mechanism of short pitch corrugation using a downscale V-Track test rig. Tribol Int. 2023;180:108293.

[50] Ren F, Yang Z, Hajizad O, et al. Experimental investigation into the initiation of head check damage using v-track. 12th International Conference on Contact Mechanics and Wear of Rail/Wheel Systems; 2022 Sep 4–7, Melbourne, VIC, Australia.
[51] Jaschinski A, Chollet H, Iwnicki S, et al. The application of roller rigs to railway vehicle dynamics. Veh Syst Dyn. 1999;31:345–392. doi:10.1076/vesd.31.5.345.8360
[52] Oregui M, Li Z, Dollevoet R. An investigation into the vertical dynamics of tracks with monoblock sleepers with a 3D finite-element model. Proc Inst Mech Eng, Part F: J Rail Rapid Transit. 2016;230:891–908. doi:10.1177/0954409715569558
[53] Perić D, Owen D. Computational model for 3-D contact problems with friction based on the penalty method. Int J Numer Methods Eng. 1992;35:1289–1309. doi:10.1002/nme.1620350609
[54] Courant R, Friedrichs K, Lewy H. On the partial difference equations of mathematical physics. IBM J Res Dev. 1967;11:215–234. doi:10.1147/rd.112.0215
[55] Zhang P, Li S, Núñez A, et al. Multimodal dispersive waves in a free rail: numerical modeling and experimental investigation. Mech Syst Signal Process. 2021;150:107305. doi:10.1016/j.ymssp.2020.107305
[56] Kang B, Riedel C, Tan C. Free vibration analysis of planar curved beams by wave propagation. J Sound Vib. 2003;260:19–44. doi:10.1016/S0022-460X(02)00898-2
[57] Baxy A, Prasad R, Banerjee A. Elastic waves in layered periodic curved beams. J Sound Vib. 2021;512:116387. doi:10.1016/j.jsv.2021.116387
[58] Grassie S, Gregory R, Harrison D, et al. The dynamic response of railway track to high frequency vertical excitation. J Mech Eng Sci. 1982;24:77–90. doi:10.1243/JMES_JOUR_1982_024_016_02
[59] Thompson D. Wheel-rail noise generation, part III: rail vibration. J Sound Vib. 1993;161:421–446. doi:10.1006/jsvi.1993.1084
[60] Daubechies I, Lu J, Wu H-T. Synchrosqueezed wavelet transforms: An empirical mode decomposition-like tool. Appl Comput Harmon Anal. 2011;30:243–261. doi:10.1016/j.acha.2010.08.002
[61] Muller S. A linear wheel–track model to predict instability and short pitch corrugation. J Sound Vib. 1999;227:899–913. doi:10.1006/jsvi.1999.2981
[62] Remington PJ. Wheel/rail noise—Part IV: rolling noise. J Sound Vib. 1976;46:419–436. doi:10.1016/0022-460X(76)90864-6
[63] Zhao X, Li Z, Dollevoet R. The vertical and the longitudinal dynamic responses of the vehicle–track system to squat-type short wavelength irregularity. Veh Syst Dyn. 2013;51:1918–1937. doi:10.1080/00423114.2013.847466
[64] Grassie S, Kalousek J. Rail corrugation: characteristics, causes and treatments. Proc Inst Mech Eng, Part F: J Rail Rapid Transit. 1993;207:57–68. doi:10.1243/PIME_PROC_1993_207_227_02
[65] He C, Yang Z, Zhang P, et al. A finite element thermomechanical analysis of polygonal wear. In: Orlova, A, Cole, D, editors. The IAVSD international symposium on dynamics of vehicles on roads and tracks. Saint Petersburg (Russia): Springer; 2021. p. 533–541.
[66] Yang Z, Zhang P, Moraal J, et al. An experimental study on the effects of friction modifiers on wheel–rail dynamic interactions with various angles of attack. Railway Eng Sci. 2022;30:360–382. doi:10.1007/s40534-022-00285-y
[67] Wang Z, Lei Z. Trend analysis of rail corrugation on the metro based on wheel–rail stick-slip characteristics. Veh Syst Dyn. 2023;62:1–30.
[68] Molodova M, Li Z, Núñez A, et al. Parametric study of axle box acceleration at squats. Proc Inst Mech Eng, Part F: J Rail Rapid Transit. 2015;229:841–851. doi:10.1177/0954409714523583
[69] Yang Z, Boogaard A, Chen R, et al. Numerical and experimental study of wheel-rail impact vibration and noise generated at an insulated rail joint. Int J Impact Eng. 2018;113:29–39. doi:10.1016/j.ijimpeng.2017.11.008
[70] Yang Z, Li Z. Numerical modeling of wheel-rail squeal-exciting contact. Int J Mech Sci. 2019;153-154:490–499. doi:10.1016/j.ijmecsci.2019.02.012